


Delineating the shape of COat Protein complex-II coated membrane bud

Sanjoy Paul ^a, Anjon Audhya ^b and Qiang Cui ^{a,c,*}^aDepartment of Chemistry, Boston University, Boston, MA 02215, USA^bDepartment of Biomolecular Chemistry, University of Wisconsin-Madison, Madison, WI 53706, USA^cDepartments of Physics and Biomedical Engineering, Boston University, Boston, MA 02215, USA*To whom correspondence should be addressed: Email: qiangcui@bu.edu

Edited By Ivet Bahar

Abstract

Curvature-generating proteins that direct membrane trafficking assemble on the surface of lipid bilayers to bud transport intermediates, which move protein and lipid cargoes from one cellular compartment to another. However, it remains unclear what controls the overall shape of the membrane bud once curvature induction has begun. In vitro experiments showed that excessive concentrations of the COPII protein Sar1 promoted the formation of membrane tubules from synthetic vesicles, while COPII-coated transport intermediates in cells are generally more spherical or lobed in shape. To understand the origin of these morphological differences, we employ atomistic, coarse-grained (CG), and continuum mesoscopic simulations of membranes in the presence of multiple curvature-generating proteins. We first characterize the membrane-bending ability of amphipathic peptides derived from the amino terminus of Sar1, as a function of interpeptide angle and concentration using an atomistic bicelle simulation protocol. Then, we employ CG simulations to reveal that Sec23 and Sec24 control the relative spacing between Sar1 protomers and form the inner-coat unit through an attachment with Sar1. Finally, using dynamical triangulated surface simulations based on the Helfrich Hamiltonian, we demonstrate that the uniform distribution of spacer molecules among curvature-generating proteins is crucial to the spherical budding of the membrane. Overall, our analyses suggest a new role for Sec23, Sec24, and cargo proteins in COPII-mediated membrane budding process in which they act as spacers to preserve a dispersed arrangement of Sar1 protomers and help determine the overall shape of the membrane bud.

Keywords: membrane remodeling, COPII, Helfrich Hamiltonian, protein transport

Significance Statement

Lipid membrane remodeling is crucial to many cellular processes. While tremendous progress has been made regarding how proteins generate local membrane deformations, such as bending and pore formation, it is less well understood how specific global membrane deformations are generated by the collective impacts of multiple proteins. For example, the COPII protein Sar1 leads to membrane tubulation under in vitro conditions, while together with other COPII components such as Sec23 and Sec24, Sar1 protomers generate spherical membrane vesicles. By integrating multiscale simulations that span atomistic and continuum scales, we illustrate how Sec23, Sec24, and cargo proteins function as spacers to ensure a diluted membrane surface coverage of Sar1 protomers which is crucial to the spherical budding of the membrane.

Introduction

COat Protein complex II (COPII) is a multiprotein molecular machinery that orchestrates the export of newly synthesized proteins from the endoplasmic reticulum (ER) via membrane-enclosed transport carriers (1). The complex consists of various isoforms of Sar1, Sec23, Sec24, Sec13, and Sec31, which are thought to assemble into a multilayered coat structure on the cytoplasmic face of discrete ER subdomains known as transitional ER. Sar1 initiates the membrane budding process when it becomes activated by transitioning from a guanosine diphosphate (GDP)-bound state to a guanosine triphosphate (GTP)-bound state by the guanine nucleotide exchange

factor Sec12 (2, 3). Subsequently, Sar1 together with Sec23–Sec24 heterodimers forms the inner-coat layer (4–6) on the membrane bud, whereas Sec13–Sec31 produces an outer cage-like layer (7, 8) to complete COPII coat formation. These membrane-bound, cargo laden carriers generally adopt a spherical or multilobed shape that are roughly ~50 to 200 nm in diameter (9). With the help of Sec16 and members of the TANGO1 family, multiple COPII-coated carriers can adopt a “beads-on-a-string” conformation to accommodate bulky procollagens (10, 11). However, in vitro experiments have demonstrated that Sar1 in the presence of GTP forms an organized lattice structure on giant unilamellar vesicles (GUVs), resulting in

Competing Interest: The authors declare no competing interests.**Received:** March 13, 2024. **Accepted:** July 10, 2024

© The Author(s) 2024. Published by Oxford University Press on behalf of National Academy of Sciences. This is an Open Access article distributed under the terms of the Creative Commons Attribution-NonCommercial License (<https://creativecommons.org/licenses/by-nc/4.0/>), which permits non-commercial re-use, distribution, and reproduction in any medium, provided the original work is properly cited. For commercial re-use, please contact reprints@oup.com for reprints and translation rights for reprints. All other permissions can be obtained through our RightsLink service via the Permissions link on the article page on our site—for further information please contact journals.permissions@oup.com.

the formation of membrane tubules (12, 13). This shape is noticeably different from the structure of COPII-coated transport carriers found inside living organisms. Further, this indicates that Sar1 alone cannot produce the spherical shape of a membrane bud. Therefore, the molecular origin of the shape of COPII-coated carriers remains poorly understood.

Regulation of the spatiotemporal accumulation of COPII proteins is crucial to drive cargo export from the ER. Our recent study highlighted the formation of the inner-coat layer as the rate-limiting step for the cargo transport process (14). We also demonstrated the molecular mechanism of membrane binding and bending activity of inner-coat protein Sar1 in a nucleotide state- and concentration-dependent manner (15). Despite these advances, what regulates the shape of membrane buds induced by COPII needs to be understood in more detail. Conventionally, it is considered that Sec23 (16) functions as a GTPase-activating protein (GAP), facilitating the hydrolysis of GTP on Sar1, whereas Sec24 (17) is involved in cargo binding. However, in the absence of Sar1, cargo export persists through the continued action of Sec23–Sec24 in a phase separated state (18). These findings suggest that Sec23–Sec24 complexes may play hitherto unrecognized roles in the process of membrane budding.

Sar1 inserts its amphipathic amino-terminal helix into the membrane to induce local positive curvature (15, 19). While a single Sar1 protein can locally deform the membrane, how multiple Sar1 molecules sculpt the membrane into distinct shapes remains unknown. The consequence of multiple curvature-inducing inclusions on membrane has been shown to produce a diverse array of morphologies such as tubes, corkscrew, disc, caveolae, etc. (20, 21). In the context of COPII-mediated membrane budding, relevant membrane shapes are tubules under *in vitro* conditions and more spherical under *in vivo* conditions. To comprehend the topology of the membrane bud formed by COPII, it is crucial to establish how the membrane responds to the multiple types of proteins involved.

In this study, we employ atomistic, coarse-grained (CG), and continuum mechanics-based simulations to elucidate the molecular mechanism of how the inner-coat layer shapes the membrane bud. Since the amphipathic amino-terminal helix is the curvature-inducing region of Sar1, we arrange multiple such peptides on the membrane and study their collective membrane bending activities. First, we compare the relative bending activities of a GTP bound Sar1 dimer vs. the amino-terminal peptide dimer in the absence of the rest of the protein using the atomistic bicelle simulation protocol. Then, we provide a quantitative estimate of the magnitude of curvature induction as a function of relative orientation of the amino-terminal peptides and their concentration. We also investigate the membrane binding ability of Sec23 and Sec24 using MARTINI-based CG model. Finally, we utilize the dynamic triangulated surface (DTS) simulation framework to explore the relationship between the surface coverage of Sar1 and the shape of the membrane bud. Taken together, our model suggests a new role for Sec23, Sec24, and cargo proteins in COPII-mediated membrane budding process in which they participate as spacers to control the relative distribution of Sar1 proteins on the lipid bilayer surface, which is critical for the spherical development of the membrane bud.

Results

Comparative assessment of the membrane-bending activity of the amino-terminal amphipathic helix of Sar1 in the presence and absence of the rest of the protein

Since the simulation of a large number of Sar1 protomers on a lipid membrane is costly at the atomistic level, we first analyze to

what degree the membrane-bending activity of Sar1 can be captured with only the amphipathic helix in the amino terminus (15). GTP bound Sar1 dimer (h-GTP dimer) produces significant positive curvature on the membrane, transforming the flat-shaped bicelle (Fig. 1A) into a highly bent dome-shaped structure (Fig. 1C). The height of phosphate mid-plane changes by ~ 4 nm as a consequence of this transition. However, when the amphipathic (Fig. 1D) helices are present alone (arrangement-1) without the rest of the protein, the magnitude of curvature induction is dramatically reduced (Fig. 1E and F). Although the protein segment that causes curvature induction is the same for both cases, we observe a stark contrast in the extent of membrane bending.

According to the hydrophobic insertion mechanism of protein-induced membrane bending (22), shallow inclusion of amphipathic helices of proteins is most effective for generating positively curved membrane deformations. Therefore, to explain the differential bending activity of the Sar1 amphipathic helices, we study the time evolution of the penetration depth of the peptides into a periodically continuous membrane. While the h-GTP dimer exhibits 40% penetration depth (as defined by Paul et al. (15)), the amphipathic helix increases the penetration depth up to 65% within ~ 100 ns when present in isolation (Fig. 1G). This deeper membrane penetration in the absence of the rest of the protein reduces the magnitude of partitioning of hydrophobic/hydrophilic residues at the membrane-water interface. While the h-GTP dimer displays $\mu \sim 1$ (Eqn. 1, Supplementary Material), the isolated peptides (arrangement-1) lead to μ significantly < 1 (Fig. 1H). This indicates that in the absence of the rest of the protein, the amphipathic helix inserts into the membrane so deeply that it brings some of its hydrophilic residues into the membrane. As a result, the interleaflet stress, which arises due to the hydrophobic/hydrophilic partitioning at the membrane water interface, becomes reduced and therefore does not bend the membrane significantly.

In addition to the excess penetration of the peptides, another contributing factor in this context can be the relative orientation of the peptides on the membrane surface (Fig. 1B). The distribution of the interpeptide angle (θ) in the h-GTP dimer is sharply peaked around $\sim 105^\circ$ whereas the peptides in isolation following arrangement-1 exhibit a broad distribution of θ (Fig. S2A, Supplementary Material). We further characterize this orientational dissimilarity by computing the ratio of the end distances (d_1 and d_2) of the peptide pair. In the case of a serial arrangement of the peptides d_1/d_2 will be $2d$ where d is the length of a single helix (~ 3.5 nm in the case of Sar1), and in the case of a parallel arrangement, d_1/d_2 should be 1. The high value of d_1/d_2 observed for the h-GTP dimer indicates a serial-like arrangement of the helix-pair while the significantly lower value of d_1/d_2 for the peptides in isolation indicates rather different arrangements (Fig. 1I). To estimate the effect of the interhelix orientation on the membrane curvature induction, we perform bicelle simulations in the presence of two peptides while restraining the interpeptide angle to be 180° (peptide-arrangement-2). The angular restraint is not observed to enhance the degree of membrane bending (Fig. 1J). Therefore, the relative orientation of the amphipathic peptides does not significantly impact the membrane-bending activity. This suggests that curvature induction by a large assembly of the amphipathic peptides can be modeled without considering specific relative orientation (*vide infra*).

The magnitude of membrane curvature induction is proportional to the concentration of the embedded peptides

In this section, we study the impact of the peptide concentration on the magnitude of membrane curvature induction. From the previous

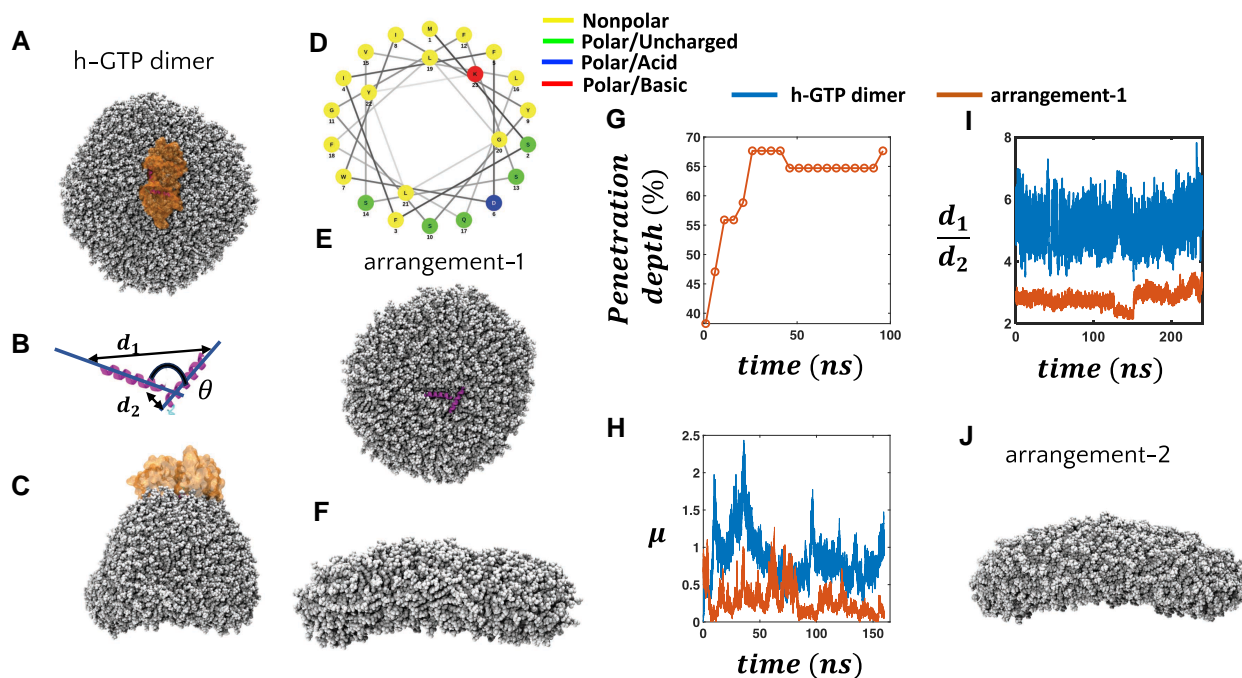


Fig. 1. Isolated amphipathic regions of Sar1 diminish its capacity to bend the membrane. (A) Top view of h-GTP dimer protein on membrane bicelle. The amphipathic helix is shown in “NewCartoon” representation. The protein is depicted in “Surface” representation and the membrane is shown in van der Waals (VDW) representation. (B) Arrangement of the helix-pair (residues 1 to 23) derived from the amino-terminal amphipathic region in h-GTP dimer. End distances of the peptide pair is represented by d_1 and d_2 and the interpeptide angle is θ . (C) Side view of the h-GTP dimer membrane system after ~ 248 ns simulation revealing a highly bent shaped membrane as a consequence of high curvature induction. (D) Helical wheel diagram of the amino-terminal amphipathic helix of h-GTP Sar1 where different colors represent different residue types. (E) Top view of the membrane bicelle system with peptide-arrangement-1 (isolated amphipathic peptide case). (F) Snapshot of the membrane bicelle with peptide-arrangement-1 after 250 ns of simulation. Time evolution of (G) membrane penetration depth and (H) μ (see Eqn. 1, Supplementary Material) for the h-GTP dimer and peptide-arrangement-1 in the presence of continuous membrane. (I) d_1/d_2 as a function of time in case of membrane bicelle simulation in the presence of h-GTP dimer and peptide-arrangement-1. (J) Snapshot of the membrane bicelle system in the presence of peptide-arrangement-2 where θ is restrained to 180° .

section, it is clear that two copies of the amphipathic peptide derived from the h-GTP dimer are unable to generate significant membrane curvature irrespective of their relative orientation. With one more amphipathic helix (peptide-arrangement-3) as shown in Fig. 2A, the magnitude of membrane curvature increases from $\sim 0.012 \pm 0.0006 \text{ nm}^{-1}$ (arrangement-1 and -2) to $0.013 \pm 0.003 \text{ nm}^{-1}$ (Fig. 2B). With six peptides (arrangement-4) distributed around the center of the bicelle (Fig. 2C), we observe strong bending of the membrane, leading to a vesicular cap like structure (Fig. 2D and Fig. S1, Supplementary Material) similar to that induced by the h-GTP dimer with a curvature of $\sim 0.025 \pm 0.002 \text{ nm}^{-1}$ (Fig. 2E). Thus, the bicelle simulations demonstrate that peptide assemblies induce membrane curvature in a concentration-dependent manner. Analysis of inter peptide angles reveals a broad distribution (50 to 180°), further confirming the lack of any strong correlation between membrane-bending activity and interpeptide orientation (Fig. S2B and C, Supplementary Material). As a control simulation, we study a bicelle system covered with a total of 18 peptides (Fig. S3, Supplementary Material). Surprisingly, in this case, we do not observe any significant membrane bending. By the end of ~ 250 ns of simulation, many peptides are located at the highly curved edges of the bicelle, and they propagate the stress induced by hydrophobic insertion throughout the membrane. As a result, the net interleaflet stress is minimal and no curvature induction is observed.

Sar1 serves as a tether connecting Sec23–Sec24 to create the inner-coat layer

We next study the binding of different protein components from the inner-coat layer to the membrane, moving toward a more

realistic description of COPII. To address this question in a computationally effective manner we adopt the CG MARTINI models, which were successfully employed to model protein (23) and liquid droplet (24)-mediated remodeling of membranes. Here, we first investigate the binding of Sec23 and Sec24 separately to the membrane. Both proteins detach from the membrane rather quickly (tens of nanoseconds) during the simulation despite initial placement on the membrane surface (Fig. 3A to D). These observations are consistent with the model that Sar1 acts as an anchor to bring Sec23 and Sec24 to the membrane surface and generate the inner-coat layer. Indeed, in a simulation with a Sar1–Sec23–Sec24 trimer on the membrane (Fig. 3E to F), Sec23 and Sec24 securely attach to Sar1, thereby maintaining their binding to the membrane and producing a cohesive unit. Subsequently, we attempt to simulate a more realistic inner-coat layer by increasing the number of repeating units of Sar1–Sec23–Sec24 from 1 to 2, 4, and 8. When the number of Sar1–Sec23–Sec24 trimer units is 2, we do not observe spontaneous protein–protein association among the trimer units due to dilution of the protein concentration (Fig. S4, Supplementary Material). However, as we increase the number of trimer units we observe more trimer–trimer associations. In the case of eight trimer repeating units, we observe that a few Sar1 proteins stay out of the membrane plane as a consequence of crowding (Fig. 3G). Overall, we observe a stable binding of the inner-coat components to the membrane where proteins are dynamically coupled with each other. We further evaluate the spacing between the Sar1 proteins in the presence and absence of Sec23 and Sec24 by measuring the distances (d_{amino}) between their amino-terminal amphipathic segments (Fig. 3H). In

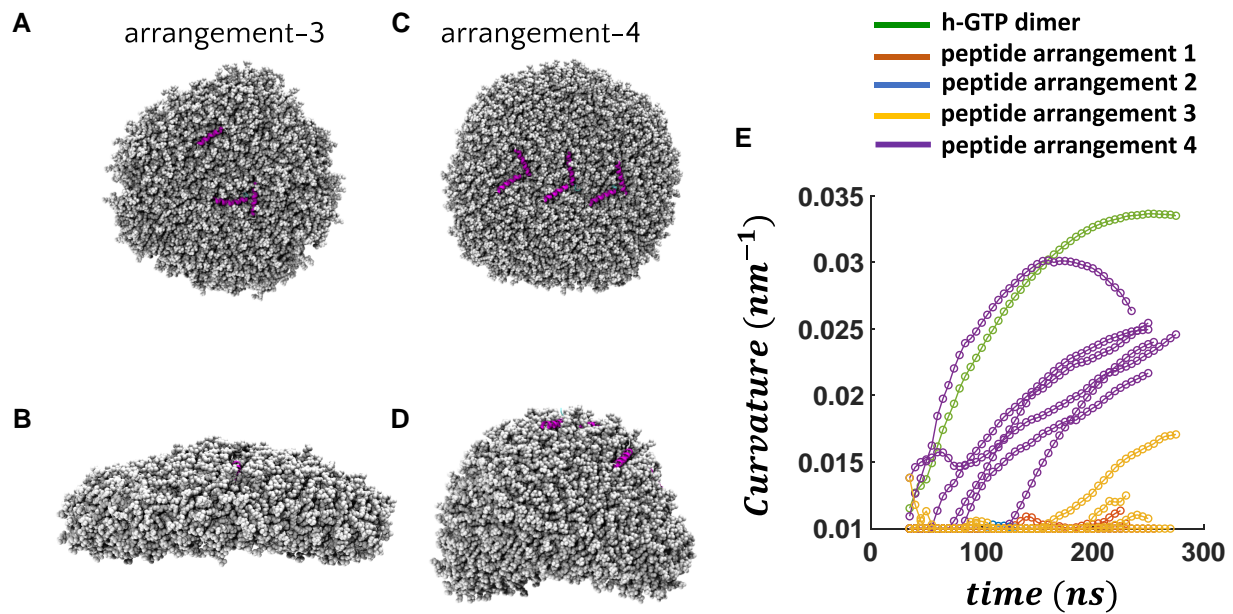


Fig. 2. Curvature induction on the membrane as a function of peptide concentration. (A) Initial (top) and (B) final (side) snapshots of a tri-peptide assembly (peptide-arrangement-3) on a membrane bicelle after ~ 250 ns simulation (replica-1). (C and D) Initial and final snapshots from replica-1 of peptide-arrangement-4. (E) Time evolution of membrane curvature in all the cases of peptide arrangements including multiple replica simulations of peptide-arrangement-1, -3, and -4 and h-GTP dimer protein. h-GTP dimer protein exhibit highest curvature followed by peptide-arrangement-4. Peptide-arrangement-1 to -2 show lowest curvature induction. Final snapshots of remaining replica simulations are shown in Fig. S1, Supplementary Material.

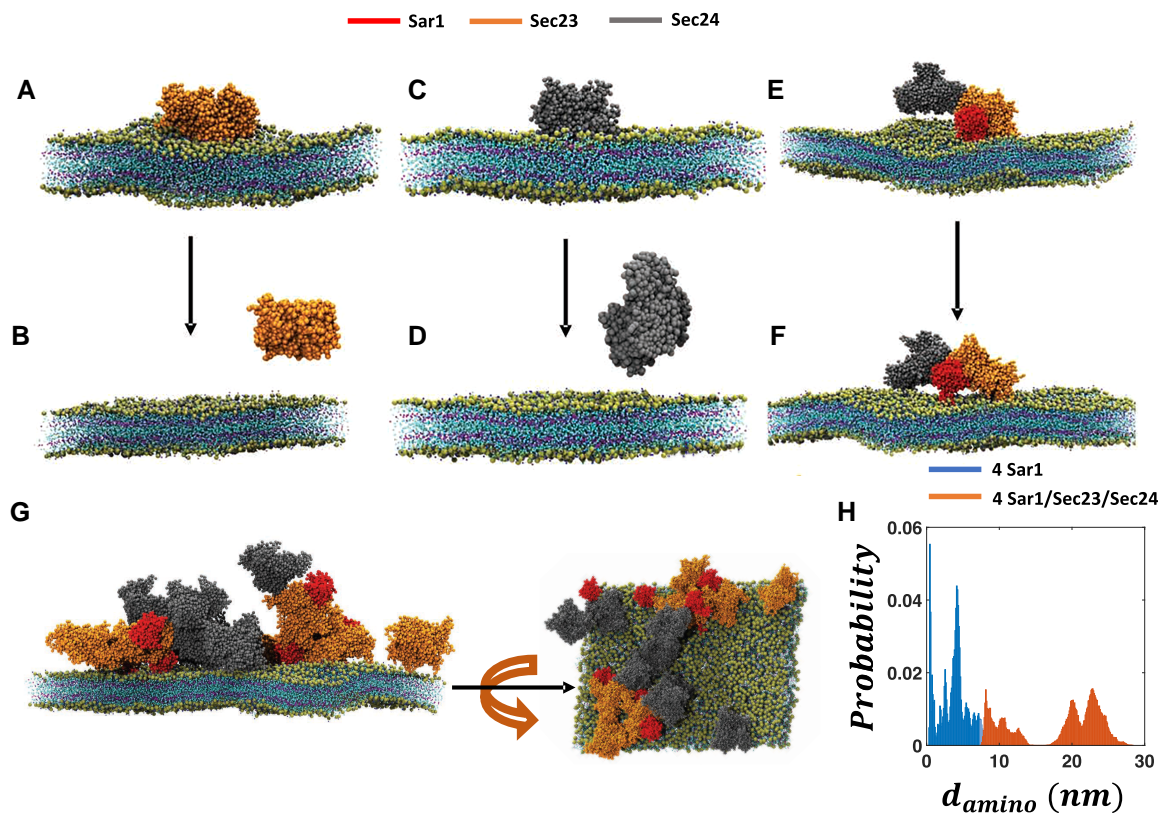


Fig. 3. Simulating the inner-coat layer using MARTINI-based description. Initial ($t = 0$) and final ($t \sim 2 \mu\text{s}$) snapshots of (A and B) Sec23, (C and D) Sec24, and (E and F) Sar1-Sec23-Sec24 trimer in the presence of membrane. Sec23 and Sec24 individually fail to maintain a stable attachment with the membrane but with the help of Sar1 it remain bound to the membrane surface. (G) Top and side views of the eight repeating units of Sar1-Sec23-Sec24 trimer. (H) Probability distribution of d_{amin0} estimated from the simulations of Sar1 tetramer in the absence of Sec23 and Sec24 and four trimer repeating units of Sar1-Sec23-Sec24.

the absence of Sec23 and Sec24, the Sar1 tetramer exhibits strong interprotein binding (Fig. S4, Supplementary Material) resulting in d_{amino} values in the range of 0 to 10 nm. In the presence of Sec23 and Sec24, d_{amino} increases significantly (~8 to 30 nm). The role of Sec23–Sec24 as spacers is robust with respect to the initial arrangement of protein configurations (Fig. S5, Supplementary Material). It is important to note that we consider only the structured part of Sec24 in our simulation. The amino terminal (residues 1 to 132) of Sec24 is intrinsically disordered and not included in our model; it is expected to further separate Sar1 protomers due to entropic repulsion. Thus, Sec23 and Sec24 serve as spacers in the inner-coat layer to separate Sar1 proteins from one another and prevent them from coassembling with one another. In addition to Sec23 and Sec24, the bulky cargo proteins that are being packaged may also serve as spacers (25). In the next section, we explore the consequence of including spacers between the curvature-generating proteins on the shape of the generated membrane bud using DTS simulations. The MARTINI simulations described in this section not only reveal the spacing between the Sar1 protomers in the presence of Sec23 and Sec24 but also provide a basis to establish the connection between the length scales considered in DTS and atomistic simulations. The simulations also reveal that structured regions of Sec23 and Sec24 cannot bind to the membrane and induce curvature. This is an experimentally testable hypothesis that is important to examine in the future to better define the roles of these proteins in COPII-mediated transport.

The effect of spacers on the shape of the membrane bud

Here, we describe how the spatial arrangement of curvature-generating proteins impacts the shape of the induced membrane bud employing the DTS simulation protocol. DTS simulations have been previously used to study the transformation of a membrane vesicle into tubes, discs, and other shapes when curvature induction takes place anisotropically (20, 26, 27). With a flat membrane patch under constant tension, isotropic curvature-inducing inclusions have been shown to produce pearled tubule-like budding when the surface coverage of the proteins exceeds a certain threshold value (28, 29). Using the atomistic bicelle simulations, we observe that isotropic curvature induction is the key characteristic in the case of Sar1-mediated membrane remodeling where the relative orientation of its amphipathic helices does not affect the magnitude of curvature induction. Results from the previous section also suggest that Sec23 and Sec24 maintain the spatial separation of Sar1 proteins. Based on these findings, we develop a mesoscopic model of the inner-coat layer on a triangulated membrane mesh where protein-containing vertices (blue region) have positive intrinsic curvatures ($c_0 = 1.0 \text{ d}^{-1}$) isotropically coupled to the Helfrich term. These curvature-inducing vertices represent Sar1 protomers while other vertices represent the membrane ($c_0 = 0 \text{ d}^{-1}$). In this case, we observe tubular budding of the membrane with one or multiple tubules (Fig. 4A). This condition resembles that in *in vitro* GUVs coated with Sar1, where tubular budding is commonly observed (12). A fraction of the protein-containing vertices turns into a tubular shape while the rest remains flat surrounding the tubular region.

Next, to model the presence of Sec23 and Sec24, we include spacers (red) uniformly distributed in the protein-containing region. With 5% spacer, we observe a pearled tubule-like shape of the membrane bud (Fig. 4B). The spacers occupy both tubular and flat protein-containing vertices. Due to the incorporation of

spacers, only one tubule is generated in four trajectories and a small spherical budding is observed in traj-2. Upon increasing the fraction of spacers from 5 to 15%, the shape of the membrane bud becomes more spherical in nature (Fig. 4C). A spherical shape is observed in almost all cases of membrane buds with a constricted neck. Only in the case of traj-2, a doubly pearled tubule is generated. Further increasing the spacer content to 25% leads to a perfectly spherical membrane bud (Fig. 4D). Thus, increasing the concentration of spacers alters tubular budding into a more spherical budding. When spacer content exceeds a certain threshold the membrane budding no longer takes place. While 50% spacer leads to a reduced size of the buds, 75% spacer does not lead to any budding during the Monte Carlo (MC) simulations (Fig. S8, Supplementary Material). This is consistent with an earlier study where the curvature-generating proteins were observed to fail to generate membrane buds when the surface coverage on the membrane is below a threshold value (28).

In the absence of volume and area compressibility, membrane budding is accompanied by intense deformation of the overall shape because of the propagation of the stress due to the fluid nature of the membrane (Fig. S9, Supplementary Material). In this case, a larger number of spacers also yields a more spherical membrane bud. To generate membrane budding, uniform distribution of the spacers is crucial. When the spacers are clustered together we do not observe prominent buds (Fig. S10, Supplementary Material). We also study the effect of anisotropic curvature induction on the shape of membrane budding (Fig. S11, Supplementary Material). With $c_{\parallel} = 1 \text{ d}^{-1}$, $c_{\perp} = 0 \text{ d}^{-1}$ and $k_{\parallel} = \kappa_B$, the membrane buds in a tubular fashion. If we turn on c_{\perp} , multiple branched spheres are generated under a strong coupling limit ($k_{\parallel/\perp} = \kappa_B$). Increasing the value of $c_{\parallel/\perp}$ results in a flat-shaped budding, which is not consistent with that observed in case of COPII in cells.

Discussion

This work demonstrates the relationship between the insertion of several amphipathic helices and the creation of specific membrane shapes. This kind of remodeling of the membrane is particularly important in the context of membrane budding triggered by protein coat assemblies (30). Here, we specifically focus on the case of COPII-mediated membrane budding. Our previous study (15) unraveled a detailed molecular picture of the membrane curvature generation by Sar1, which is known to initiate the COPII-mediated protein trafficking. This study goes beyond the description based on Sar1 and examines the impact of including other inner-coat proteins, Sec23 and Sec24, on the morphology of the membrane budding process. Our findings demonstrate that when Sar1 is densely organized without other COPII proteins, it leads to tubular membrane budding. However, when Sec23 and Sec24 are added, they do not directly contribute to the curvature induction but regulate the surface coverage of Sar1, resulting in a more spherical shape of the bud. Therefore, our results suggest an additional role for Sec23, Sec24, and cargo proteins during COPII transport carrier formation, where they regulate the spacing between Sar1 proteins and thereby facilitate the formation of spherical membrane carriers. This is also supported by recent cryo-EM derived structures showing that Sar1–Sec23–Sec24 trimer units appear as randomly oriented patches on vesicles (25) in contrast to uniformly distributed lattices found on the membrane tubules (5). The amino-terminal intrinsically disordered region (IDR) of Sec24, which is not considered in this study, is composed of 70 hydrophilic (13 of which are charged)

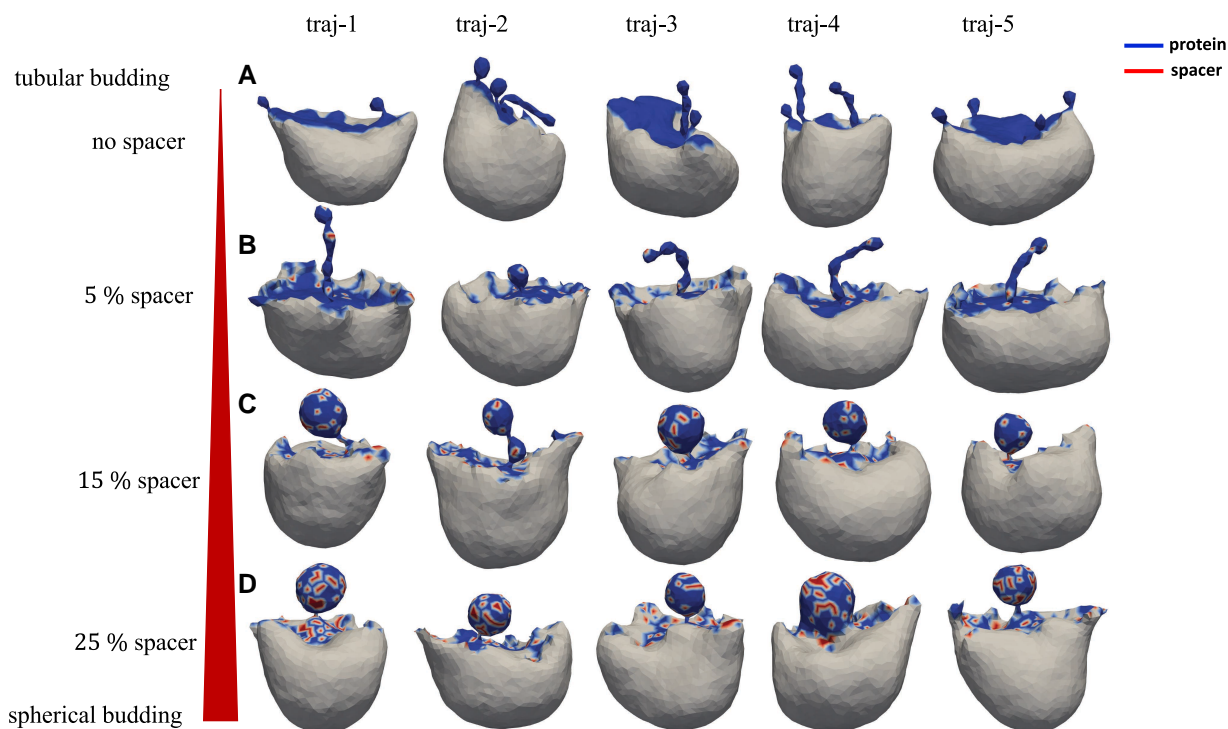


Fig. 4. MC simulations of triangulated membrane mesh where 20% vertices are occupied by proteins. The shape of the membrane mesh after 5×10^5 MC steps in five parallel runs in the presence of (A) no spacer, (B) 5%, (C) 15%, and (D) 25% spacers. The thickness of the red bar is proportional to the number of spacers. The white region is the protein-free membrane surface facing a volume (K_V) and area (K_A) compressibility of $10 \kappa_B$.

and 62 hydrophobic residues. It is unclear whether this IDR region helps Sec24 attach to the membrane. However, our simulations indicate that Sec23 and the structured region of Sec24 require Sar1 to maintain their stable attachment with the membrane and thereby form the inner-coat layer. According to our previous studies (15, 19), Sar1 binds to the membrane in both GDP- and GTP-bound states, but only creates positive membrane curvature in the GTP-bound state. Therefore, Sar1 together with Sec23 and Sec24 are able to be associated with the membrane prior to any curvature induction. Afterwards, Sec12 exchanges GDP bound to Sar1 with GTP, which triggers Sar1 to induce curvature on the membrane. However, due to the presence of Sec23, Sec24, and cargo proteins, Sar1 protomers remain scattered on the membrane surface with disordered orientations, leading to spherical budding of the membrane.

Membrane-active amphipathic peptides are known to insert and can lead to pore formation (31, 32). The C-terminal amphipathic helices of complexin have been shown to produce a stable pore in the lipid bilayer when the number of peptides reaches 12 (33). There are just seven hydrophilic residues out of 23 in the amino-terminal helix of Sar1. We observe that the amphipathic peptides derived from Sar1 are embedded horizontally to the membrane plane without stretching across despite containing a large amount of hydrophobic residues. The spontaneous transition of a membrane bicelle to a vesicular intermediate triggered by curvature-generating protein has been demonstrated previously using the MARTINI model (34). Here, we establish the dependence of the concentration of amphipathic peptide on the magnitude of curvature induction on membrane bicelle (Fig. 2). We also reveal that the relative membrane sculpting efficiency of amphipathic peptides decreases in the absence of the entire protein segment. In the case of BAR (35, 36) domains and the ESCRT machinery (37), proteins form an intrinsically curved

filament, which is key to the process of membrane bending by these proteins. On the contrary, the lack of dependency of the membrane curvature induction on the interpeptide angle indicates that the curvature induction is isotropic in the case of COPII. Our DTS simulations also reveal that isotropic curvature induction on the protein-bound vertices is essential to producing spherical membrane bud at optimal spacer concentration.

The conventional mechanism of cargo transport through COPII-coated membrane vesicles has been challenged by two recent experiments (38–40). These results suggest that COPII localizes at the neck of the membrane bud, defining a boundary between ER and ER-Golgi intermediate compartments (ERGIC). Further, the inhibition of Sar1 reduced the recruitment of Sec23 on the ER membrane and thus disrupted the formation of a proper COPII assembly (39). Our MARTINI-based simulations also support this finding by showing that Sar1 recruits Sec23–Sec24 to form the inner-coat layer. However, the mechanism by which such a ring-shaped COPII collar can produce a membrane bud remains unclear.

In summary, we offer a mechanistic overview of the complex interplay between multiple proteins from COPII family in regulating the shape of the coated membrane surface. We cover a broad range of length scales by employing atomistic, MARTINI, and Helfrich Hamiltonian-based mesoscale simulations to establish the role of spacer proteins in producing spherical membrane buds. Our atomistic simulations indicate that the membrane penetration depth of the amphipathic helices increase significantly in the absence of the rest of the protein segment (Fig. 1G). This can be tested experimentally by fluorescence quenching-based assays as described in (19) where one can monitor the fluorescence quenching of a Trp residue within the amino-terminal amphipathic helix by quenchers present at various depths of the membrane. Based on our simulations, we also predict that Sar1

in the presence of Sec23 and Sec24 sculpt spherical/lobe shaped budding rather than tubules on GUVs, which can also be investigated experimentally. In our study, we focus on the inner-coat proteins Sar1, Sec23, and Sec24, which are considered to be the key players in the membrane budding process at the subdomains of ER. In addition to the inner-coat layer, Sec13 and Sec31 form the outer-coat layer, which has a cage-like structure and promotes vesicle fission (41). It is not clear whether the highly bent outer-coat layer also contributes to the curvature induction and membrane budding process. An intriguing possibility is that interactions between the inner and outer coat protein facilitate appropriate spacing between Sar1 protomers to drive the budding of spherical transport carriers. Although our approach of modeling the inner-coat layer is sufficient to explain the shapes of re-modeled membranes in both *in vitro* and *in vivo* conditions, it is important in the next step to directly consider the roles of Sec13 and Sec31 in this process.

Materials and methods

We perform simulations at three different length scales which are atomistic, CG, and mesoscopic (see Table S1, Supplementary Material for the summary of MD simulations conducted). First, we assess the membrane penetration depth of the Sar1 amphipathic helices by performing atomistic simulations using a continuous membrane bilayer. We follow the protocol described in Paul et al. (15) to perform the atomistic membrane simulations. The h-GTP dimer model of Sar1 is first introduced into an atomistic lipid bilayer (10 nm × 10 nm) containing 66% DOPC, 21% DOPE, 8% DOPS, and 5% DOPA; that is, a 13% anionic membrane. We ignore the remaining protein and solvent and only take into account the amino-terminal amphipathic helix (residues 1 to 23) embedded in the membrane bilayer. The system is then resolved and re-ionized to maintain the physiological (0.15 M) salt concentration and to make the system charge-neutral. Following minimization and equilibration, NPT simulations are carried out for 160 ns with the Nosé–Hoover thermostat and Parrinello–Rahman barostat (semiisotropic pressure coupling) to control the temperature and pressure of the system. All simulations are performed using GROMACS (42, 43) version 2018.3 and the CHARMM36m (44) force field with the TIP3P explicit solvent model. We estimate the magnitude of the partitioning of the hydrophobic/hydrophilic residues of the amphipathic helices at the membrane-water interface by a quantity μ (see Supplementary Material text for definition).

Next, we perform simulations with the membrane bicelle for ~250 ns to evaluate the extent of membrane bending by these amphipathic helices. We model the bicelle system by replicating the continuous membrane system along +X: -X and +Y: -Y directions using the *gmx genbox* utility followed by the deletion of membrane segments near the edges to break the membrane continuity along X and Y (see Supplementary Material text and Paul et al. (15) for details). To demonstrate the statistical robustness of our membrane bicelle simulation strategy, we conduct six independent replica simulations for peptide-arrangement-4, four for peptide-arrangement-3, and three for peptide-arrangement-1. All simulations began with identical starting coordinates but had different starting velocities. VMD version 1.9.3 (45) is used for visualization and analysis. The helical wheel diagram is constructed using NetWheels (46).

Afterwards, to demonstrate the effect of Sec23 and Sec24 on the relative spacing between Sar1 proteins on the membrane surface, we perform CG simulations using the MARTINI 3 model with Sar1 (Figs. S3 and S4, Supplementary Material) and multiple units of

the Sar1–Sec23–Sec24 trimer on a lipid bilayer. We convert the atomistic models of Sar1–Sec23–Sec24 (PDB code: 6GNI (5)) trimer into MARTINI3.0 (47) model using *martinize2* (48) with the elastic bond force constant of 1300 kJ/mol/nm² and a decay factor 0.8. After building the MARTINI model of the proteins, we construct a ~40 nm × 30 nm membrane bilayer with 87% DOPC and 13% DOPS lipid molecules and place the protein molecules on top using the *insane* tool. Then, we add water beads and Na⁺/Cl⁻ to neutralize the system and maintain a physiological salt concentration. The simulation box size is ~40 nm × 30 nm × 30 nm. After energy minimization and short equilibration, a ~2 to 5 μ s production run is carried out with the equilibrated configuration. In this step, V-rescale thermostat and Parrinello–Rahman barostat are used with the same τ_p . The time step in the MARTINI simulations is 20 fs.

Finally, we carry out the MC simulation of the DTS model following the strategy described by Ramakrishnan et al. (21, 49) In this simulation the membrane dynamics is governed by the Helfrich Hamiltonian at the mesoscopic length scale where the membrane is considered as a surface discretized by triangles (see Supplementary Material for more details). The presence of curvature-inducing proteins is represented by vertices that have intrinsic nonzero curvatures. Here, instead of using the formalism developed by Ramakrishnan et al., we utilize isotropic curvature induction as discussed by Pezeshkian et al. (28). Vertex movement and link flips are considered as the MC moves. We allow nematic exchange between protein (blue) and spacers (red) while no nematic exchange is allowed between membrane and protein/spacer. A total of 5×10^5 MC steps are carried out. For comparison, we also perform DTS simulations using anisotropic curvature induction condition. The total number of vertices in the membrane vesicle is 2030, 20% of which are occupied by proteins (Sar1). Among the protein-containing vertices, we place spacers representing Sec23/Sec24 with varying amounts (5 to 75%). We use *paraview* (50) to visualize the membrane in the form of the triangulated mesh where surface representation is selected and the color scheme is based on the phases of the vertices. Nonprotein-containing vertices (gray) belong to phase 2 whereas proteins (blue) and spacers (red) containing vertices belong to phases 1 and 3, respectively.

Acknowledgments

We thank Dr. Ramakrishnan Natesan for the discussion regarding the mesoscale model of membranes. We also thank Dr. Xiao-Han Li for useful comments on the manuscript. We are grateful to Soubhik Mondal for helping us with fortran codes during the early stages of DTS simulations. This manuscript was posted on a preprint server: <https://doi.org/10.1101/2024.02.13.580145>.

Supplementary Material

Supplementary material is available at PNAS Nexus online.

Funding

The work is supported in part by the NSF grant to QC (CHE-2154804). This work used Delta at the National Center for Supercomputing Application (NCSA) through allocation MCB110014 from the Advanced Cyberinfrastructure Coordination Ecosystem: Services & Support (ACCESS) program (51), which is supported by the U.S. National Science Foundation (NSF) under the Office of Advanced Cyberinfrastructure awards #2138259, #2138286, #2138307, #2137603, and #2138296. A part of the computational work was performed on the Shared Computing Cluster

which is administered by Boston University's Research Computing Services (URL: www.bu.edu/tech/support/research/).

Author Contributions

S.P., A.A., and Q.C. designed research; S.P. performed research; S.P. and Q.C. analyzed data; and S.P., A.A., and Q.C. wrote the paper.

Data Availability

Scripts for analyzing atomistic and CG MD trajectories and the codes for DTS simulations are freely available at : <https://github.com/Sanjoy-Paul/membrane-budding/>.

References

- Hughes H, Stephens DJ. 2008. Assembly, organization, and function of the COPII coat. *Histochem Cell Biol.* 129:129–151.
- d'Enfert C, Wuestehube LJ, Lila T, Schekman R. 1991. Sec12p-dependent membrane binding of the small GTP-binding protein sar1p promotes formation of transport vesicles from the ER. *J Cell Biol.* 114(4):663–670.
- Lee MCS, et al. 2005. Sar1p N-terminal helix initiates membrane curvature and completes the fission of a COPII vesicle. *Cell.* 122(4):605–617.
- Bi X, Corpina RA, Goldberg J. 2002. Structure of the Sec23/24–Sar1 pre-budding complex of the COPII vesicle coat. *Nature.* 419(6904):271–277.
- Hutchings J, Stancheva V, Miller EA, Zanetti G. 2018. Subtomogram averaging of COPII assemblies reveals how coat organization dictates membrane shape. *Nat Commun.* 9(1):1–8.
- Shaywitz DA, Espenshade PJ, Gimeno RE, Kaiser CA. 1997. COPII subunit interactions in the assembly of the vesicle coat. *J Biol Chem.* 272(41):25413–25416.
- Bi X, Mancias JD, Goldberg J. 2007. Insights into COPII coat nucleation from the structure of sec23* sar1 complexed with the active fragment of sec31. *Dev Cell.* 13(5):635–645.
- Hutchings J, et al. 2021. Structure of the complete, membrane-assembled COPII coat reveals a complex interaction network. *Nat Commun.* 12(1):2034.
- Matsuoka K, et al. 1998. COPII-coated vesicle formation reconstituted with purified coat proteins and chemically defined liposomes. *Cell.* 93(2):263–275.
- Raote I, et al. 2018. Tango1 builds a machine for collagen export by recruiting and spatially organizing COPII, tethers and membranes. *Elife.* 7:e32723.
- Raote I, et al. 2020. A physical mechanism of tango1-mediated bulky cargo export. *Elife.* 9:e59426.
- Long KR, et al. 2010. Sar1 assembly regulates membrane constriction and ER export. *J Cell Biol.* 190(1):115–128.
- Hariri H, Bhattacharya N, Johnson K, Noble AJ, Stagg SM. 2014. Insights into the mechanisms of membrane curvature and vesicle scission by the small GTPase Sar1 in the early secretory pathway. *J Mol Biol.* 426(22):3811–3826.
- Kasberg W, Luong P, Swift KA, Audhya A. 2023. Nutrient deprivation alters the rate of COPII subunit recruitment at ER subdomains to tune secretory protein transport. *Nat Commun.* 14(1):8140.
- Paul S, Audhya A, Cui Q. 2023. Molecular mechanism of GTP binding-and dimerization-induced enhancement of Sar1-mediated membrane remodeling. *Proc Natl Acad Sci USA.* 120(8):e2212513120.
- Yoshihisa T, Barlowe C, Schekman R. 1993. Requirement for a GTPase-activating protein in vesicle budding from the endoplasmic reticulum. *Science.* 259(5100):1466–1468.
- Wendeler MW, Paccaud J-P, Hauri H-P. 2007. Role of sec24 isoforms in selective export of membrane proteins from the endoplasmic reticulum. *EMBO Rep.* 8(3):258–264.
- Kasberg W, et al. 2023. The Sar1 GTPase is dispensable for COPII-dependent cargo export from the ER. *Cell Rep.* 42(6):112635.
- Hanna MG, et al. 2016. Sar1 GTPase activity is regulated by membrane curvature. *J Biol Chem.* 291(3):1014–1027.
- Ramakrishnan N, Ipsen JH, Kumar PBS. 2012. Role of disclinations in determining the morphology of deformable fluid interfaces. *Soft Matter.* 8(11):3058–3061.
- Ramakrishnan N, Kumar PBS, Radhakrishnan R. 2014. Mesoscale computational studies of membrane bilayer remodeling by curvature-inducing proteins. *Phys Rep.* 543(1):1–60.
- Campelo F, McMahon HT, Kozlov MM. 2008. The hydrophobic insertion mechanism of membrane curvature generation by proteins. *Biophys J.* 95(5):2325–2339.
- Mandal T, Spagnolie SE, Audhya A, Cui Q. 2021. Protein-induced membrane curvature in coarse-grained simulations. *Biophys J.* 120(15):3211–3221.
- Mondal S, Cui Q. 2022. Coacervation of poly-electrolytes in the presence of lipid bilayers: mutual alteration of structure and morphology. *Chem Sci.* 13(26):7933–7946.
- Pyle E, Zanetti G, 17 January, 2024. Cryo-electron tomography reveals how COPII assembles on cargo-containing membranes. *bioRxiv* 2024.01.17.576008. <https://doi.org/10.1101/2024.01.17.576008>, preprint: not peer reviewed.
- Ramakrishnan N, Kumar PBS, Ipsen JH. 2013. Membrane-mediated aggregation of curvature-inducing nematogens and membrane tubulation. *Biophys J.* 104(5):1018–1028.
- Kumar G, Ramakrishnan N, Sain A. 2019. Tubulation pattern of membrane vesicles coated with biofilaments. *Phys Rev E.* 99(2):022414.
- Pezeshkian W, Ipsen JH. 2019. Fluctuations and conformational stability of a membrane patch with curvature inducing inclusions. *Soft Matter.* 15(48):9974–9981.
- Pezeshkian W, Ipsen JH. 2024. Mesoscale simulation of biomembranes with FreeDts. *Nat Commun.* 15(1):548.
- Stachowiak JC, Brodsky FM, Miller EA. 2013. A cost-benefit analysis of the physical mechanisms of membrane curvature. *Nat Cell Biol.* 15(9):1019–1027.
- Kabelka I, Vácha R. 2021. Advances in molecular understanding of α -helical membrane-active peptides. *Acc Chem Res.* 54(9):2196–2204.
- Ulmschneider JP, Ulmschneider MB. 2018. Molecular dynamics simulations are redefining our view of peptides interacting with biological membranes. *Acc Chem Res.* 51(5):1106–1116.
- Courtney KC, et al. 2022. The complexin C-terminal amphipathic helix stabilizes the fusion pore open state by sculpting membranes. *Nat Struct Mol Biol.* 29(2):97–107.
- Bhaskara RM, et al. 2019. Curvature induction and membrane remodeling by FAM134B reticulon homology domain assist selective ER-phagy. *Nat Commun.* 10(1):2370.
- Arkhipov A, Yin Y, Schulten K. 2008. Four-scale description of membrane sculpting by bar domains. *Biophys J.* 95(6):2806–2821.
- Arkhipov A, Yin Y, Schulten K. 2009. Membrane-bending mechanism of amphiphysin N-bar domains. *Biophys J.* 97(10):2727–2735.
- Mandal T, Lough W, Spagnolie SE, Audhya A, Cui Q. 2020. Molecular simulation of mechanical properties and membrane activities of the ESCRT-III complexes. *Biophys J.* 118(6):1333–1343.

-
- 38 Shomron O, et al. 2021. COPII collar defines the boundary between ER and ER exit site and does not coat cargo containers. *J Cell Biol.* 220(6):e201907224.
- 39 Weigel AV, et al. 2021. ER-to-Golgi protein delivery through an interwoven, tubular network extending from ER. *Cell.* 184(9):2412–2429.
- 40 Malis Y, Hirschberg K, Kaether C. 2022. Hanging the coat on a collar: same function but different localization and mechanism for COPII. *BioEssays.* 44(10):2200064.
- 41 Zanetti G, Pahuja KB, Studer S, Shim S, Schekman R. 2012. COPII and the regulation of protein sorting in mammals. *Nat Cell Biol.* 14(1):20–28.
- 42 Abraham MJ, et al. 2015. Gromacs: high performance molecular simulations through multi-level parallelism from laptops to supercomputers. *SoftwareX.* 1:19–25.
- 43 Berendsen HJC, van der Spoel D, van Drunen R. 1995. Gromacs: a message-passing parallel molecular dynamics implementation. *Comput Phys Commun.* 91(1–3):43–56.
- 44 Huang J, et al. 2017. Charmm36m: an improved force field for folded and intrinsically disordered proteins. *Nat Methods.* 14(1):71–73.
- 45 Humphrey W, Dalke A, Schulten K. 1996. VMD: visual molecular dynamics. *J Mol Graph.* 14(1):33–38.
- 46 Ribeiro Mol A, Castro MS, Fontes W. 2024. NetWheels: a web application to create high quality peptide helical wheel and net projections. *J Bioinform Syst Biol.* 7:98–100. .
- 47 Souza PCT, et al. 2021. A general purpose force field for coarse-grained molecular dynamics. *Nat Methods.* 18(4):382–388.
- 48 Kroon PC, et al. 2022. Martinize2 and vermouth: unified framework for topology generation. arXiv, arXiv:2212.01191, preprint: not peer reviewed.
- 49 Ramakrishnan N, Kumar PBS, Ipsen JH. 2010. Monte carlo simulations of fluid vesicles with in-plane orientational ordering. *Phys Rev. E.* 81(4):041922.
- 50 Ahrens J, Geveci B, Law C, Hansen C, Johnson C. 2005. 36-paraview: an end-user tool for large-data visualization. *Vis Handb.* 717:50038–1.
- 51 Boerner TJ, Deems S, Furlani TR, Knuth SL, Towns J. 2023. Access: Advancing innovation: NSF’s advanced cyberinfrastructure coordination ecosystem: services & support. *Pract Exp Adv Res Comput.* 173–176.